A bidimensional fluid system with competing interactions: spontaneous and induced pattern formation

2004 J. Phys.: Condens. Matter 16 S3769

(http://iopscience.iop.org/0953-8984/16/38/001)

INSTITUTE OF PHYSICS PUBLISHING JOURNAL OF PHYSICS: CONDENSED MATTER

J. Phys.: Condens. Matter **16** (2004) S3769–S3789 PII: S0953-8984(04)79834-3

A bidimensional fluid system with competing interactions: spontaneous and induced pattern formation

A Imperio and L Reatto

Istituto Nazionale di Fisica della Materia and Dipartimento di Fisica, Università degli Studi di Milano, via Celoria 16, 20133 Milan, Italy

Received 23 April 2004
Published 10 September 2004
Online at stacks.iop.org/JPhysCM/16/S3769
doi:10.1088/0953-8984/16/38/001

Abstract

In this paper we present a study of pattern formation in bidimensional systems with competing short-range attractive and long-range repulsive interactions. The interaction parameters are chosen in such a way as to allow us to analyse two different situations: the spontaneous pattern formation due to the presence of strong competing interactions on different length scales and the pattern formation as a response to an external modulating potential when the system is close to its Lifshitz point. We compare different Monte Carlo techniques showing that the parallel tempering technique represents a promising approach for the study of such systems and we present detailed results for the specific heat and the structural properties. We also present random phase approximation predictions concerning spontaneous pattern formation (or microphase separation), as well as linear response theory predictions concerning the induced pattern formation due to the presence of an external modulating field. In particular we observe that the response of our systems to external fields is much stronger than the response of a Lennard-Jones fluid.

(Some figures in this article are in colour only in the electronic version)

1. Introduction

Spontaneous pattern formation can easily be observed in systems far from thermal equilibrium due to energy and matter fluxes (see [1] and references therein), but it can also be observed in equilibrium states as a result of the competition between interactions operating on different length scales [1–7]. Patterns appear both in two- and three-dimensional systems; in the last few decades, bidimensional or quasi-bidimensional systems have also grown in importance due to the possibility of technological applications. In particular, the possibility of manipulating pattern formation through the application of external fields has attracted great interest. Typical experiments involve fluid films exposed to interfering multiple laser beams or ferrofluids in

magnetic fields, with the result that the external agent can manipulate the morphology of clusters as well as the nature of the transitions (e.g. laser induced freezing) [8–10].

The competing terms are typically due to a short-range attraction, which tends to induce a macroscopic phase separation, and a longer-range repulsion, present in addition to the hard core contribution, which causes a frustration of the system favouring the formation of smaller clusters of particles. The short-range attraction is often explained in terms of van der Waals forces, while the long-range repulsion is often related to effective or actual dipolar interactions as in Langmuir monolayers and in magnetic films [3, 11, 12]. Another source of long-range repulsion is a screened Coulomb interaction of charged macroparticles (see [5, 13] and references therein).

In this paper we present continuum simulation results on a bidimensional system subject to an effective potential which includes competing interactions. Specific features arise if the repulsion is truly long range, like the dipolar one. We do not explore this aspect since we are interested in generic aspects of competition, so both attraction and repulsion are assumed to have a finite range. At first, the potential parameters were set for studying the spontaneous breaking of symmetry leading to pattern formation (or microphase separation) without an external field. Simulations have been done adopting different Monte Carlo techniques; in particular, the parallel tempering scheme has been explored. Finally, the parameters of interactions have been chosen so as to allow study of the pattern formation induced by an external modulating potential, when the fluid is near its Lifshitz point. In fact, it is known from previous studies [14] that specific features appear in the properties of the system even when the long-range repulsion is not strong enough to give rise to microphase separation and a normal liquid–vapour transition is present. Close to this Lifshitz point the coexistence curve is extremely flat and the region of large compressibility increases enormously compared to the normal case. Under these conditions we might expect a very large response to an external modulating field. Both cases have been analysed for different thermodynamic states.

The paper is organized as follows. In section 2 we discuss and compare different Monte Carlo techniques for simulating systems with competing interactions. Computational results are described in section 3; in section 4 we compare simulation data with theoretical predictions based on the random phase approximation and describe a very simple model for explaining why we observe different patterns as density increases. Section 5 is dedicated to the analysis of the pattern induced by an external modulating potential. A comparison with a standard Lennard-Jones fluid response is also given. In section 6 we draw conclusions.

2. Microphases: the model system and computational details

The model system studied in this paper is similar to that in [2]. Unlike the authors of [2] we have focused our attention on the thermodynamic and structural features of the system. We have analysed such quantities for a large range of temperatures, obtaining information on the microphase region and also on the transition among the ordered states and the homogeneous one. The particles interact via a spherically symmetric pairwise-additive potential which is a sum of two parts:

$$U(r) = U_{\rm sr}(r) + U_{\rm lr}(r). \tag{1}$$

The short-range contribution $U_{\rm sr}$ is the hard disc potential, while the long-range one is

$$U_{\rm lr}(r) = -\frac{\epsilon_{\rm a}\sigma^2}{R_{\rm a}^2}\exp\left(-\frac{r}{R_{\rm a}}\right) + \frac{\epsilon_{\rm r}\sigma^2}{R_{\rm r}^2}\exp\left(-\frac{r}{R_{\rm r}}\right), \tag{2}$$

where r is the interparticle distance, σ is the hard disc diameter; the subscripts a and r refer to the 'attraction' and 'repulsion', so $R_{\rm a}$, $R_{\rm r}$ and $\epsilon_{\rm a}$, $\epsilon_{\rm r}$ are respectively the ranges and the

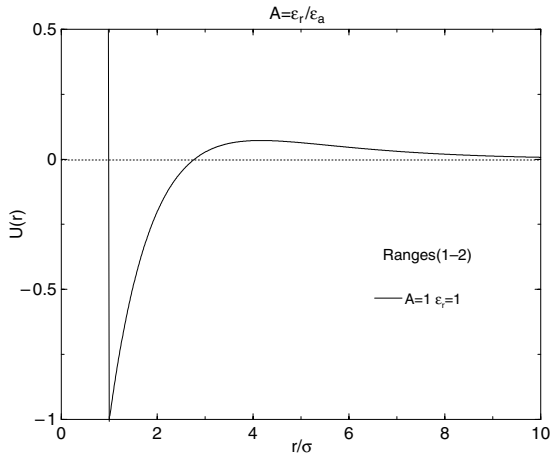

Figure 1. The interaction potential for a pair of particles. The ranges of the interactions are defined in the text.

strengths of the long-range interactions. In the first part of the paper we study the case of $\epsilon_a = \epsilon_r$, so $\int_0^\infty U_{lr}(r)\,d\mathbf{r} = 0$. We have performed a few control computations for the ranges $R_a = 2\sigma$ and $R_r = 4\sigma$ as in [2], but all the results reported here have interaction ranges equal to $R_a = 1\sigma$ and $R_r = 2\sigma$, in order to reduce the computational cost of simulations without affecting the basic physics of the system. In the figures and in all that follows we will use the reduced variables $T \equiv kT/U_c$, $U \equiv U/U_c$ (with $U_c = |U_{lr}(r = \sigma)|$, also referred to as the contact value of the potential), $\rho \equiv \langle\rho\rangle\sigma^2$ (with $\langle\rho\rangle = N/A$; N: number of particles, A: simulation box area).

We have used different strategies of simulation. First we performed computer simulations using the standard Metropolis Monte Carlo algorithm (in the following MC) [15] at fixed number of particles N, area A and temperature T, with periodic boundary conditions and the minimum image convention. We applied a spherical cut-off R_c (always smaller than half of the simulation box side); that is, we set the pair potential $U(r)$ to zero for $r \geqslant R_c$ and then we included tail corrections in the computation of the potential energy to compensate for the missing long-range part of U_{lr} due to the cut-off. We used $N = 400$, but in preliminary runs we adopted $N = 1600$ to test the effect of the finite size of the simulation box and in figure 2, for instance, we have plotted snapshots relating to a state exhibiting a striped pattern. We can see that the shape of the pattern does not change: stripes remain parallel to each other; the excess internal energy per particle is the same (within the statistical uncertainty); the wavevectors which identify the periodicity of the pattern (that we will define more precisely in section 3) are the same in the two cases and correspond to $k_p\sigma \simeq 0.60$; changes in the radial distribution function when computed with different numbers of particles are less than 2%.

Since we are dealing with systems subject rather to long-range interactions, we have tested different cut-off values within the simulations. In particular, using a cut-off that is too short, we could completely miss the features of the state, simply because the long-range repulsion becomes too weak or is even absent. In particular, at $R_c = 2.5\sigma$ (where the particles do not feel the repulsive hump of U_{lr} at all) the system displays a standard liquid–vapour phase transition when T is low; the same happens at $R_c = 3\sigma$; at $R_c = 5\sigma$ we can observe the formation of domains whose shape is mostly irregular, while at $R_c = 10\sigma$ and $R_c = 15\sigma$ striped patterns have formed, whose shape is very regular (see figure 3). As regards the last two cases, we note that an increase by 50% of the cut-off has produced an increase by ∼6% in the pattern period.

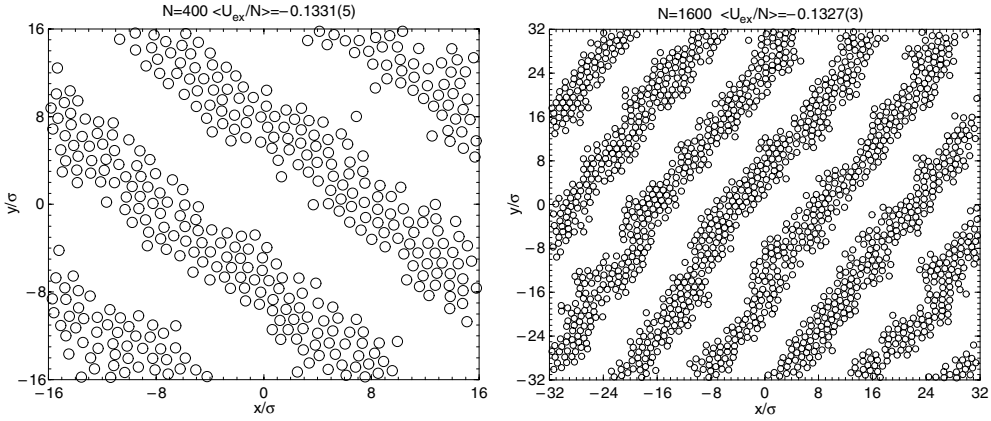

Figure 2. Snapshots relating to the state $\rho = 0.4T = 0.5$, using different numbers of particles in MC simulations. There are no relevant modifications to the shape of the striped pattern. The wavevectors connected to the periodicity of the pattern are the same in the two cases: $k_p\sigma = 0.60$.

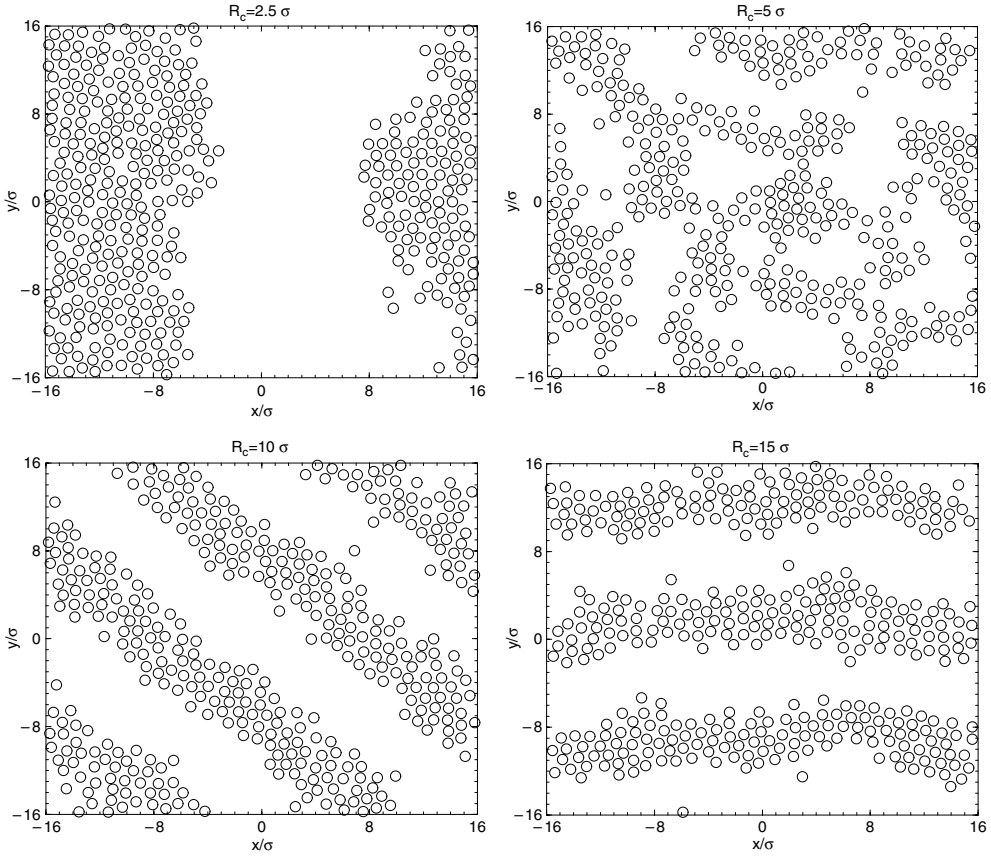

Figure 3. Snapshots relating to the state $\rho = 0.4T = 0.5$ with different cut-offs R_c.

Such a feature, however, does not affect the overall picture that can be traced as regards such phases from the present study, which is mainly aimed at characterizing general behaviour

relating to the pattern formation. Ergodicity problems were checked for by starting test runs from completely different initial conditions: we have used both homogeneous configurations (with particles set on a square lattice covering the entire simulation box) and totally segregated configurations (in which all the particles belong to the same liquid-like cluster). In all cases, the simulations converged to the same state.

The standard MC method follows a Markov chain through the configuration space. Each MC move consists of a single particle displacement and the move is accepted with probability 1 if the resulting energy change $\Delta E \leqslant 0$, and accepted with probability $\exp(-\Delta E/kT)$ otherwise. This method produces the correct equilibrium ensemble probability in the limit of infinite simulation time. Inside this scheme the passage of particles from one cluster to another is not very frequent when T is very small, so the system remains 'frozen' in a certain configuration for a long time (i.e. for many MC steps per particle). We supplemented this conventional method with additional MC moves designed to accelerate the motion through the configuration space. Thus we introduced a collective move (or cluster move) that tries to update simultaneously the position of many particles. In the following we will refer to this technique as $\mathrm{MC_{cl}}$. At this point we want to emphasize that, here and in the following, the term cluster will be used to identify a generic collection of particles irrespective of its morphology. When we intend to refer to a particular cluster morphology we will explicitly speak of circular domains (or droplets) and stripes.

In the $\mathrm{MC_{cl}}$ scheme we choose to identify the clusters using a geometrical criterion: particles i and j belong to the same cluster if their separation $d = |\mathbf{r}_i - \mathbf{r}_j| \leqslant R_0$. Typically $R_0 = 1.5\sigma$, corresponding to an attractive interaction between particles. In other words, the particles belonging to the same cluster are connected by a percolative path. Having identified the clusters, we must ensure that any cluster move will not prevent us from finding the inverse move at a later time, which means that cluster moves must not change the particle connectivity. This is achieved by displacing the centre of mass of each cluster uniformly in a box of fixed side, but forbidding cluster attachment to preserve detailed balance [16, 17]. Inside this scheme, in which we use the detailed balance principle and assume a symmetric transition matrix [18] for the probability of performing a trial move, the acceptance criterion reduces once again to $\min(1, \exp(-\Delta E))$, where ΔE is the energy change between the new and the old configurations. The collective moves represent 20% of the total.

In this way, large changes of the system can be obtained in a single MC step. Such moves are favourable mainly at low temperature where the mean displacement of a cluster can be 1–2 orders of magnitude bigger than the single-particle one. At high temperature this technique is not so effective because of the greater probability of cluster overlap. This scheme enhances the sampling of the configuration space with respect to the simple MC technique.

In addition, to be sure of sufficiently sampling the configuration space and to ensure that we were not trapped in a local minimum of the free energy landscape, we adopted the parallel tempering algorithm (PT) (see [18–20] and references therein). The PT technique was developed for dealing with the slow dynamics of disordered spin systems. The PT algorithm simultaneously simulates a set of M identical non-interacting replicas of a system, each of them at a different temperature. Periodically, a swap between configurations belonging to different replicas is attempted. The exchange is accepted in a Metropolis fashion applied to an extended ensemble which is a combination of subsystems that are NVT_i ensembles [18]. The acceptance criterion is

$$W_{m,n} = \begin{cases} 1 & \Delta_{m,n} \leqslant 0, \\ \exp(-\Delta_{m,n}) & \Delta_{m,n} > 0, \end{cases} \tag{3}$$

where $\Delta_{m,n} = (\beta_n - \beta_m)(E_m - E_n)$, with $E_m E_n$ energies of the replicas of indices m, n and β is

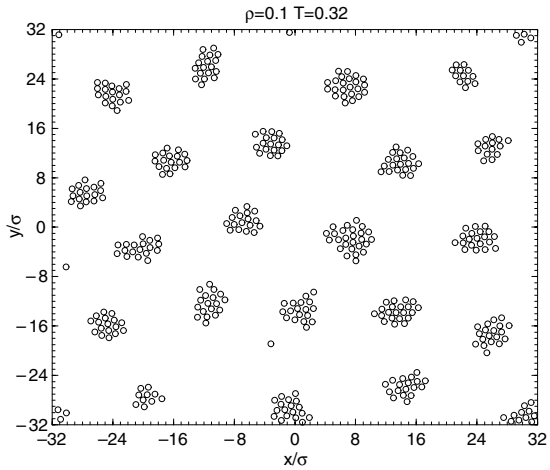

Figure 4. An example of a droplet pattern.

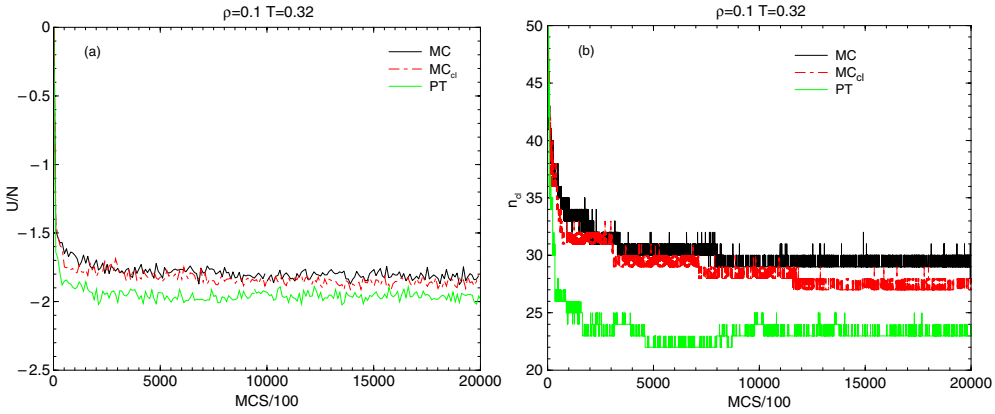

Figure 5. (a) The instantaneous potential energy per particle; (b) the number of clusters; the attempted cluster moves make up 20% of the total number of MC moves; the attempted swap moves in PT make up ∼0.05% of the total number of MC moves. MCS stands for MC steps per particle. The initial configuration was a homogeneous square lattice.

the inverse of temperature. The success of PT relies on the fact that the temperature range covers values high enough to pass every free energy barrier. The outcome of such calculations is, in principle, equilibrium configurations in the canonical ensemble at the M different temperatures. In our simulation we took $M = 31$ and we covered the range $0.32 \leqslant T \leqslant 0.92$. Each replica evolved according to an MC_{cl} scheme with attempted swap moves making up 0.05% of the total number of MC moves. We examined only exchange events between subsystems that are nearest neighbours in temperature: i and $i + 1$ [21]. Comparing PT with the techniques previously described we find that it is very efficient for improving convergence and sample equilibrium configurations, especially for the low temperature states. See, for example, figure 5 where we plotted the number of clusters and the potential energy per particle for the thermodynamic state $\rho = 0.1$ and $T = 0.32$ (a snapshot of which is shown in figure 4). In figure 6(a) we plotted the covariance relative to U/N obtained with different simulation schemes versus the distance (expressed in MC steps) between two different configurations. On each line the filled symbols

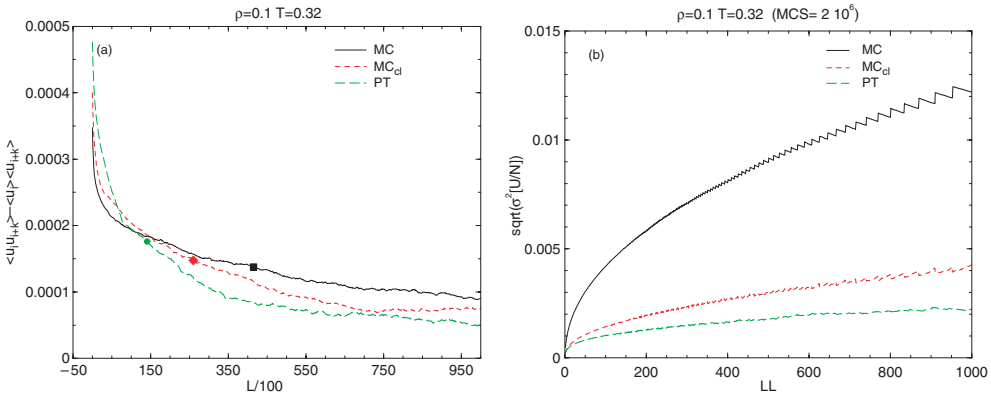

Figure 6. (a) Covariance versus distance in MCS (MC steps per particle) between configurations generated with different MC schemes; $u = (U/N)$. Filled symbols: $1/e$ decay (see the text) with respect to the initial value. (b) Estimator of variance versus length of blocks used in the data blocking scheme for the computation of statistical errors; LL is the number of configurations in each block.

mark the point where the covariance drops by a factor of $1/e$ with respect to the initial value: the configurations generated with the PT algorithm become uncorrelated faster than they do with the other methods. In figure 6(b) we plotted the estimators for the variance, using the data blocking technique, for the computation of statistical averages and errors: if the simulation is sufficiently long the estimator tends toward a constant [18]. We see that for a simulation run of fixed length, the PT curve is the flattest one; i.e., using the PT technique we need shorter runs. A typical length of our PT runs is $\sim 5 \times 10^6$ MC steps per particle.

3. Simulation results

We report our results for the interaction potential of equation (1); the parameters of the potential are $\epsilon_a = \epsilon_r = 1$, while the ranges are $R_a = 1\sigma$ and $R_r = 2\sigma$. Initial investigations were done using the standard MC algorithm, from which we located the region of the phase diagram corresponding to different pattern formation. We explored the density range $\rho = 0.1$–0.8 and the temperature range $T = 0.3$–1.0. At $T < 0.7$ we were able to observe the formation of microphases. In particular, for $\rho \lesssim 0.35$, circular domains of particles (i.e. droplets) were observed, while for $0.35 \lesssim \rho < 0.6$, liquid-like striped patterns formed. This is qualitatively in agreement with many experimental results in which, as the density increases, the cluster morphology changes to form a pattern with lower curvature [2, 3]. At higher densities, gas bubbles inside a liquid medium could be observed as a counterpart of the liquid droplets. The aim of the present computations was to characterize only the major features of the phase diagram, so we cannot exclude the possibility of the presence of some additional morphology mainly in the transition region between droplets and stripes. The characteristic dimension of the pattern is simply connected to the range of the potential: the droplet diameter as well as the stripe width is $\sim(4$–$5)\sigma$ which roughly corresponds to the location of the repulsive hump of U_{lr}. Extensive computations were done with the PT and the cluster moves technique which essentially confirmed the preliminary runs but allowed more precise computation of the thermodynamic and structural quantities of the system. In this paper we report the results relating to two particular densities, $\rho = 0.1$ and 0.4, for which the system exhibits droplet and striped patterns respectively. The simulation results given in this section were obtained adopting the PT if not otherwise specified.

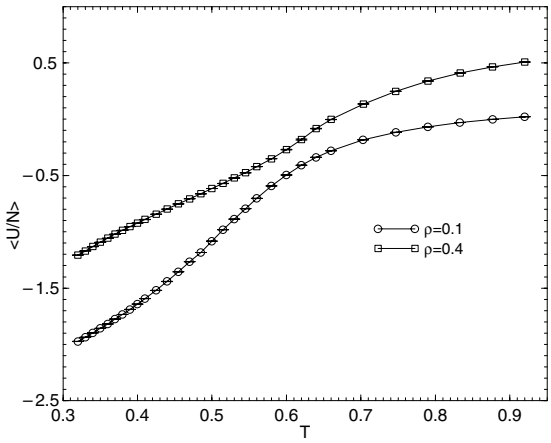

Figure 7. Simulation data for the average excess internal energy per particle at different densities. The statistical uncertainty is smaller than the symbol size. Continuous curves are only guides to the eyes.

In figure 7 we plotted the average excess internal energy per particle $\langle U/N\rangle$ for the droplet and stripe cases: at higher density the excess internal energy is less than it is in the low density case, because particles which belong to stripes at $\rho = 0.4$ feel a stronger reciprocal repulsion than they do when they are in droplets at $\rho = 0.1$. In the following section we will discuss, within a simple model, the change of cluster morphology as the density increases.

In order to identify the phase transition leading to the loss of order of the microphase region, we computed the dimensionless excess heat capacity per particle as shown in figure 8. We have computed $C_v^{\rm ex}/Nk_{\rm B}$ at constant volume in two ways:

$$\frac{C_v^{\rm ex}}{Nk_{\rm B}} = \frac{1}{Nk_{\rm B}}\frac{{\rm d}\langle U\rangle}{{\rm d}T}, \tag{4}$$

$$\frac{C_v^{\rm ex}}{Nk_{\rm B}} = \frac{1}{N}\frac{\langle U^2\rangle - \langle U\rangle^2}{(k_{\rm B}T)^2}. \tag{5}$$

Since we study the system at discrete temperatures, the derivative is approximated with finite differences, so

$$\frac{C_v^{\rm ex}(T_n)}{Nk_{\rm B}} = \frac{1}{Nk_{\rm B}}\frac{\langle U(T_{n+1})\rangle - \langle U(T_{n-1})\rangle}{T_{n+1} - T_{n-1}} \tag{6}$$

with $T_{n+1} > T_{n-1}$. In equilibrium the results from these two ways of calculating $C_v^{\rm ex}$ should agree. In the top panel of figure 8 we have shown the results relating to the second method, while a comparison between the two methods for each density is shown in the middle and bottom panels. The agreement between the two methods is quite good, suggesting that the systems have equilibrated well at all temperatures. The peaks of the specific heat identify the phase transition from the microseparated region to the homogeneous one. The corresponding transition temperatures are $T_{\rm c}^{\rm d} = 0.5$ for the droplets and $T_{\rm c}^{\rm s} = 0.62$ for the stripes. The latter case shows a particularly pronounced peak and also the snapshots of the system confirm an abrupt passage from an ordered configuration to a disordered one (see figure 9). It is interesting to note that the specific heat for $\rho = 0.4$ has a maximum at $T = 0.34$ and this seems to be connected to the freezing transition inside the stripes, as we will discuss below, treating structural quantities such as the radial distribution function $g(r)$ and the static structure factor $S(k)$.

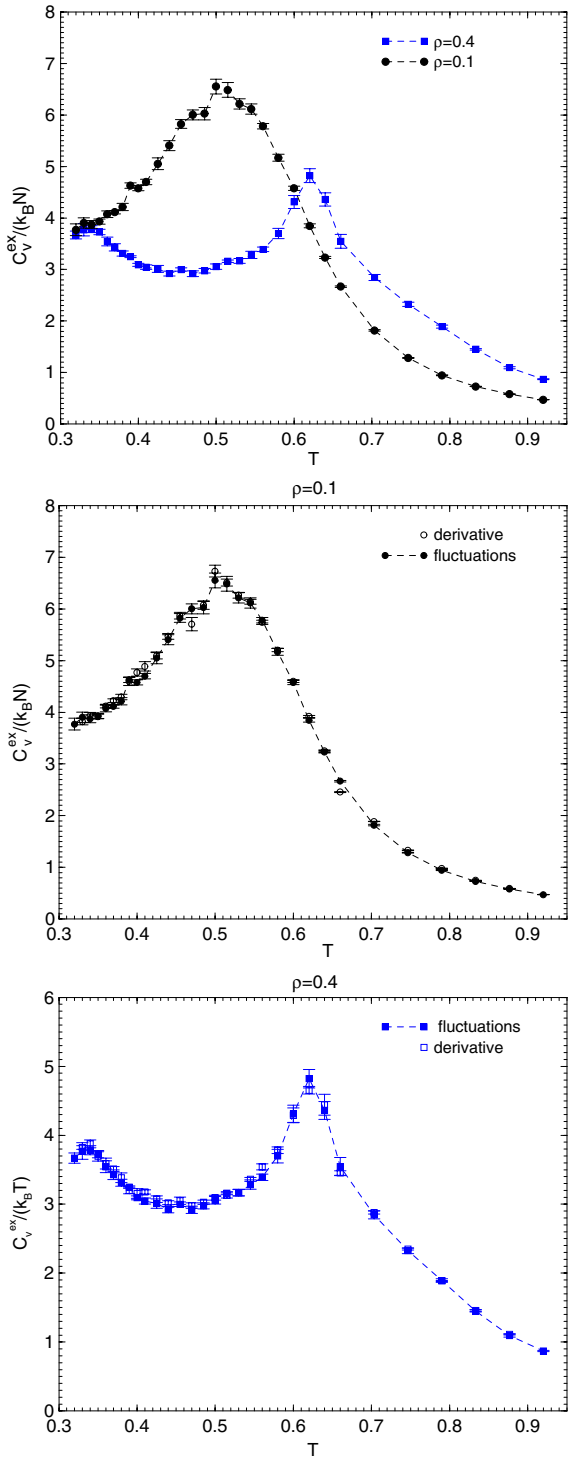

Figure 8. Upper panel: comparison of the dimensionless excess heat capacity per particle for densities $\rho = 0.1$ and 0.4 computed according to equation (5); middle and bottom panels: comparison between the results from the two methods of computing $C_v^{ex}/(k_BT)$ according to equations (5) and (4). Dashed curves are only guides to the eyes.

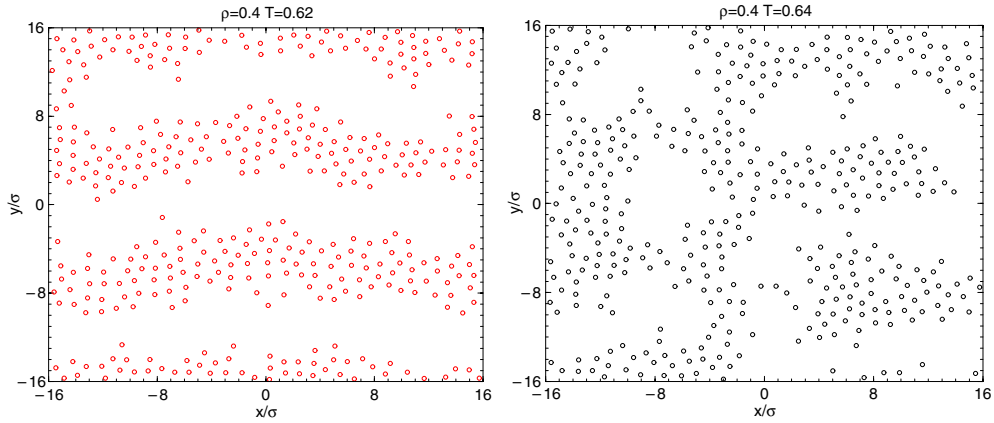

Figure 9. Snapshots relating to the microphases–homogeneous fluid transition.

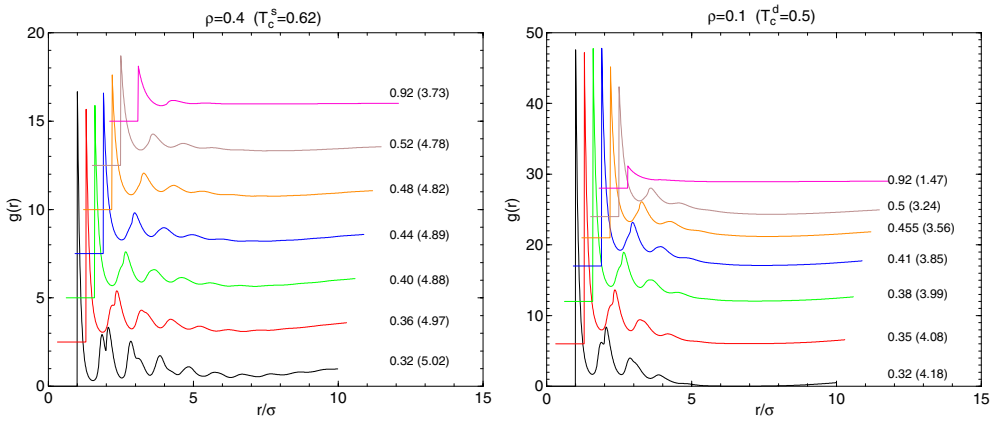

Figure 10. Left: $g(r)$ for $\rho = 0.4$; right: $g(r)$ for $\rho = 0.1$; next to the curves the temperature and (in parentheses) the coordination number are indicated; the curves are shifted for clarity. The critical temperature is also reported.

In figure 10 we have plotted $g(r)$ (computed by averaging over all the directions and normalized to the mean density of the system) for different temperatures; in the same figure we have indicated the coordination number n_c:

$$n_c = 2\pi\rho \int_0^{R_{\min}} r g(r)\, \mathrm{d}r, \tag{7}$$

in which $R_{\min}$ is the position of the first minimum. The curves are shifted for clarity; we can identify two regimes: a short-range modulation due to the local structure of the fluid and a longer-range modulation due to the microphase formation. The latter manifests itself in a shallow minimum around $\rho \sim 6\sigma$ at low temperature, which will disappear as the system becomes homogeneous at larger T. As temperature decreases, the second peak of $g(r)$ develops a shoulder which eventually grows until there is actually a peak splitting. The appearance of this shoulder has been referred to as a structural freezing precursor for both two and three dimensions [22]. The shoulder appears at $T \sim 0.38$–0.40 for droplets and at $T \sim 0.44$–0.46

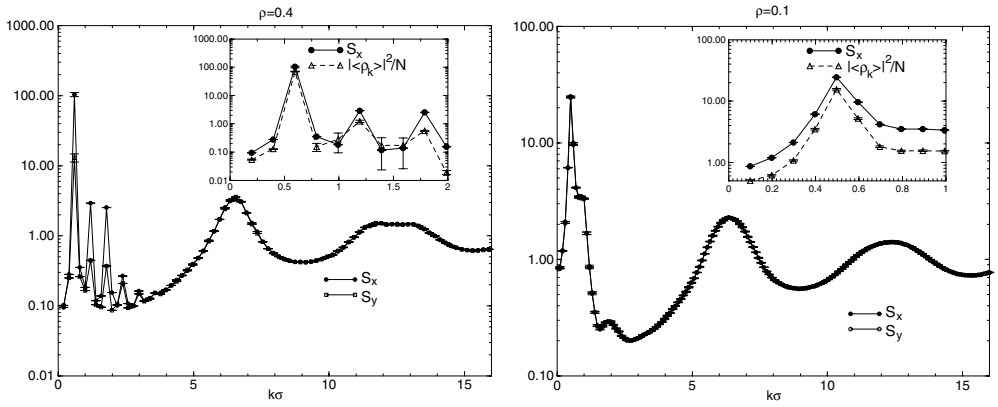

Figure 11. The static structure factor at $T = 0.36$ computed along the x and y directions for different densities. The insets show the structure factor compared with an estimator of the Fourier transform of the density profile along the same direction.

for stripes, while the splitting is clearly visible at $T = 0.32$ for droplets and $T = 0.38$ for stripes. The peak splitting is consistent with a triangular lattice of period $a \sim 1.05\,\sigma$.

The static structure factor has been calculated by explicit evaluation of the expression

$$S(\mathbf{k}) = N^{-1}\left\langle\left(\sum_i^N \cos(\mathbf{k}\cdot\mathbf{r}_i)\right)^2 + \left(\sum_i^N \sin(\mathbf{k}\cdot\mathbf{r}_i)\right)^2\right\rangle, \tag{8}$$

with $\mathbf{k}$ along different directions so, in the following, we will refer to $S_x(k)$ and $S_y(k)$ as the static structure factors with k along the x and y directions respectively. Due to the finite size of the simulation box, we can compute such a quantity only for wavevectors that are multiples of the smallest vector $k_0 = 2\pi/L_\mathrm{b}$ (L_b: simulation box side). In figure 11 we have reported the results at one temperature for the two densities studied. We can recognize two regimes. For $k\sigma < 3$ the peaks are strictly connected to the modulation of the pattern which the clusters arrange themselves in. We refer to the peaks at low k as the modulation peaks. The height of the modulation peak strongly depends on the direction of the stripes and the direction of $\mathbf{k}$ along which we are computing $S(k)$—i.e., whether the stripes are close to one of the principle axes of the simulation box or not. For instance, at $\rho = 0.4$, as plotted in figure 11, the x direction lies perpendicular to the stripes, while the y direction is parallel to them. In the inset of the same figure we have also shown a comparison between $S(k)$ and the square of the Fourier transform of the density modulation $|\langle\rho_k\rangle^2|/N$, to underline that the peaks are to a large extent due just to the density modulation. Of course, in a very long run the pattern will fluctuate, giving a uniform density, so $\langle\rho_k\rangle$ will vanish whereas $S(k)$ maintains the modulation peaks. The location of the main modulation peak corresponds to a modulation period $\lambda = 2\pi/k \sim 11\sigma$. For $k\sigma > 3$, in contrast, the behaviour of $S(k)$ is determined mainly by the structure of the fluid inside the clusters. As a matter of fact, at low temperature we can observe a flattening of the peaks at $k\sigma > 10$ until a true peak splitting occurs (at the lowest temperatures), which is just the counterpart in the Fourier space of the peak splitting observed in the radial distribution function.

Even if the interparticle interaction potential is characterized by a spherical symmetry, we see that, in the microphase region of the phase diagram, the pattern shape can show a breaking of symmetry. Such a feature is particularly evident in the stripe case where the particle domains are aligned along a fixed direction, even if such a direction is selected at random. To make this

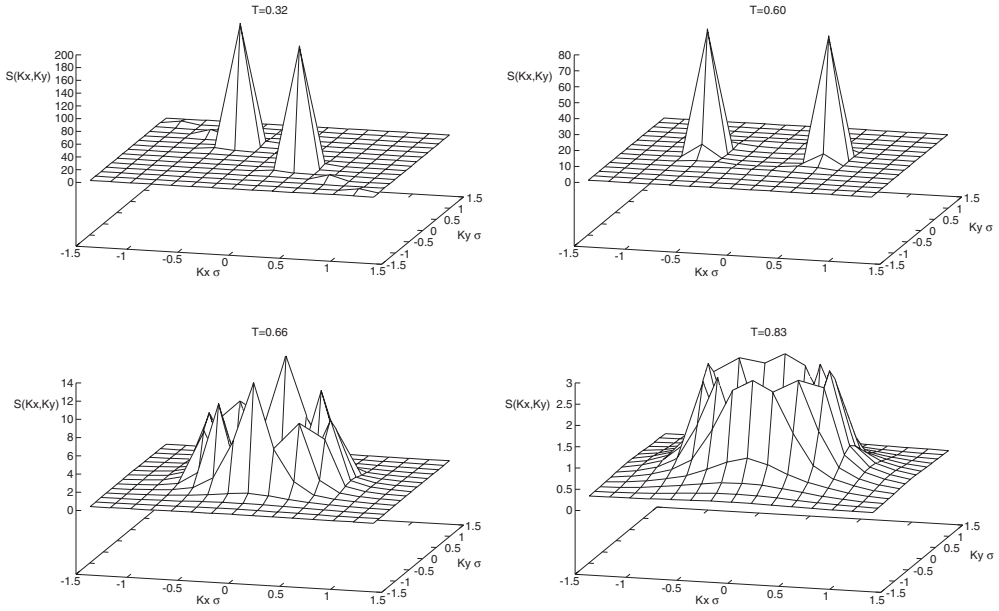

Figure 12. The structure factor at different temperatures for $\rho = 0.4$, adopting the MC_{cl} technique. Upper panels show temperatures below the critical one, while the bottom panels are for temperatures higher than T_c^s.

aspect clear we have shown in figure 12 the structure factor computed on a grid of **k** vectors (the mesh of which depends on the simulation box sides as previously explained), using the MC_{cl}, at different temperatures. Below the critical temperature (upper panels) the pattern shape has a twofold symmetry, as we can argue from the presence of a modulation peak (and the specular one) only along a single direction. At $T = 0.32$, secondary peaks can also be seen due to the harmonics. The height of the modulation peaks decreases with temperature; their width, in contrast, is limited by the finite size of the simulation cell. At temperatures higher than the critical one (bottom panels), the structure factor shape changes: modulation peaks appear in different directions until they form a ring at small k. The presence of the ring means that enhanced density fluctuations are also present at high temperatures, and their characteristic length scale is linked to the inverse of the radius of such a ring according to the formula $\lambda \sim 2\pi/k$. Some anisotropy exhibited by the height of the structure factor along the ring is still present at $T \gtrsim T_c$ and this can be interpreted as a measure of the persistence of such density fluctuations, a persistence which can be very lengthy (the data shown in figure 12 were, in fact, obtained via a simulation whose run length was 5×10^6 MC steps). Similar results are obtained with the PT technique.

4. Random phase approximation and a simple model for phase behaviour

The static structure factor $S(k)$ gives many important details on the structure of a fluid; $S(k)$, defined as

$$S(k) = 1 + \rho h(k), \tag{9}$$

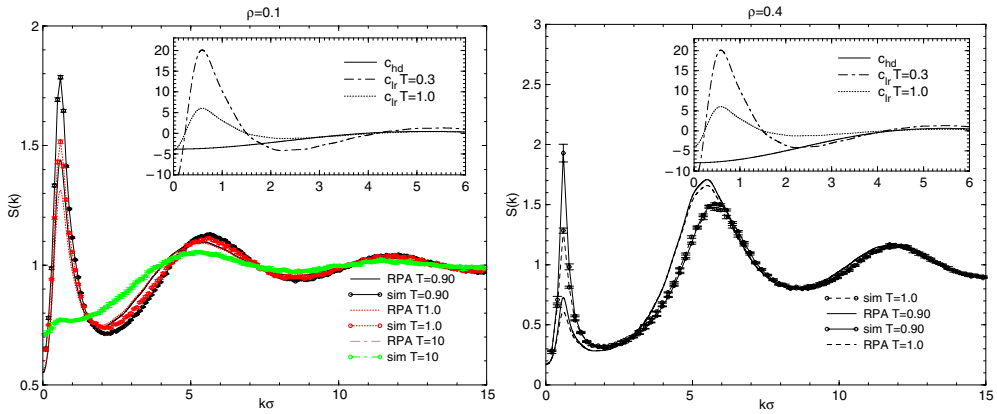

Figure 13. RPA predictions concerning the structure factor compared with simulation data for different densities and temperatures in the homogeneous regime; in the insets we show a comparison between the hard disc direct correlation function and the contribution due to the long-range term of the potential.

where $h(r)$ is the total correlation function, can also be expressed, via the Ornstein–Zernicke equation, as

$$S(k) = \frac{1}{1 - \rho c(k)}, \tag{10}$$

in which the direct correlation function $c(k)$ appears. Equation (10) is more useful because, for potentials with steep repulsion plus a weak tail, we can use the following decomposition:

$$c(k) = c_{\rm sr}(k) + c_{\rm lr}(k), \tag{11}$$

making a distinction between a short-range contribution ($c_{\rm sr}$) due to the hard disc potential and a long-range one due to $U_{\rm lr}$. For $c_{\rm sr}$ we adopted the expression given in [23], which comes from simulation data fitting. For the long-range contribution we have used the random phase approximation (RPA) $c_{\rm lr} \simeq -U_{\rm lr}(k)/k_{\rm B}T$. In figure 13 we compare this approximate structure factor for a few thermodynamic states at high temperature with simulation data. The theoretical as well as the simulation $S(k)$ exhibit a large peak for $k\sigma < 1$ which is connected at high temperature to a characteristic length scale of fluctuations which at low temperature becomes the characteristic wavevector of the patterns. The insets show a comparison between $c_{\rm hd}$ and $c_{\rm lr}$: for $k\sigma < 1$, $c_{\rm lr}$ has a much stronger dependence on k than $c_{\rm hd}$, so the structure is mainly dominated by the long-range potential (see also [24]). Simulations however show stronger density fluctuations compared with the RPA results. The agreement between the simulation and RPA as regards the modulation peak is better at higher temperature, since the approximation of a weak potential tail is better fulfilled. Within the RPA, the locus of points where $S(k)$ diverges is the spinodal that we reported in figure 14, where we also reported the critical temperature estimated for $\rho = 0.1$ and 0.4 from the specific heat. The spinodal curve is quite similar to that of a classical fluid which undergoes only a fluid–fluid separation and it exhibits a critical density around $\rho \sim 0.3$. From our preliminary simulation we found a transition from circular domains to stripe domains just around $\rho \sim 0.3$–0.35, but we have not yet explored this transition region in detail. At low T, due to competition between long-range repulsion and short-range attraction, a fluid–fluid separation is forbidden, but particles arrange themselves on smaller clusters to decrease reciprocal repulsion. On increasing the density, however, the cluster–cluster repulsive interaction is not negligible any longer, and above a

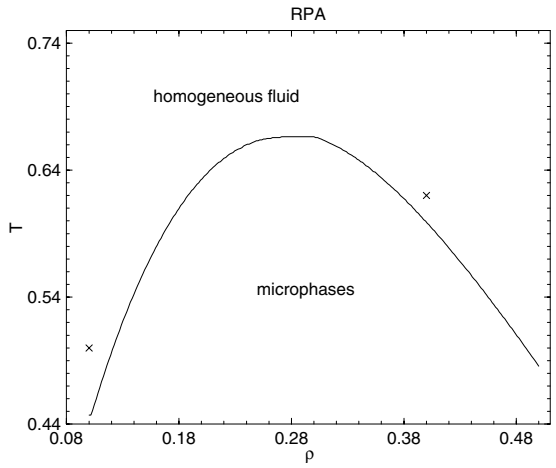

Figure 14. The spinodal curve obtained by studying the divergence of the structure factor according to equations (10) and (11). Crosses indicate simulation results obtained from the study of the specific heat (see the previous section).

certain density a new pattern becomes favoured in order to minimize repulsion, leading to a morphology change that in our case is a passage from droplets to stripes. Let us assume that the transition is dominated by energetic effects; we introduce a very simplified model in order to predict the stability of the two patterns. We treat separately the interactions among particles which belong to the same cluster and the interactions among particles belonging to different clusters, in order to clarify the role of reciprocal interaction among clusters. The first kind of interaction is indicated by the subscript c, while the latter ones are indicated by the subscript cc. The excess internal energy per particle can be expressed as

$$U^{\mathrm{ex}}/N = u_{\mathrm{c}} + \chi u_{\mathrm{cc}}, \tag{12}$$

where $\chi = N_{\mathrm{cl}} z/2$ (N_{cl}: number of clusters, z: coordination number of the clusters, i.e. 6 for droplets supposed to be on a triangular lattice and 2 for stripes supposed to be on a regularly spaced grid) is proportional to the number of first-neighbour clusters. Our goal is to compute such a quantity over the density range $\rho = 0.1$–0.5 for each pattern (droplets and stripes).

Once we have chosen the pattern, we suppose that the clusters are identical—that is, that all the droplets have the same diameter and all the stripes have the same width. We also suppose that the average distance d among clusters is fixed and set equal to the value obtained from the RPA. Since N (the total number of particles), A (the simulation box area) and d (the average distance among clusters) are fixed, we can obtain, for each pattern, the number of clusters N_{cl}, the number of particles n and the density ρ_{cl} inside each cluster and their area S_{cl}.

Approximate expressions for u_{c} and u_{cc} are

$$u_{\mathrm{c}} = (U^{\mathrm{ex}}/n)_{\mathrm{c}} = \tfrac{1}{2}\rho_{\mathrm{cl}} \int U(r) g(r)\, \mathrm{d}\mathbf{r}, \tag{13}$$

$$u_{\mathrm{cc}} = (U^{\mathrm{ex}}/n)_{\mathrm{cc}} = \frac{\rho_{\mathrm{cl}}}{S_{\mathrm{cl}}} \int_{S^1_{\mathrm{cl}}} \int_{S^2_{\mathrm{cl}}} U(r) g_n^{(2)}(\mathbf{r}^1, \mathbf{r}^2)\, \mathrm{d}\mathbf{r}^1\, \mathrm{d}\mathbf{r}^2, \tag{14}$$

where $U(r)$ is the interaction potential adopted in equation (1), the integral is over the cluster domain and the superscripts 1 and 2 underline the fact that we are referring to two different clusters. The expressions for u_{c} and u_{cc} are obtained by analogy with the excess internal

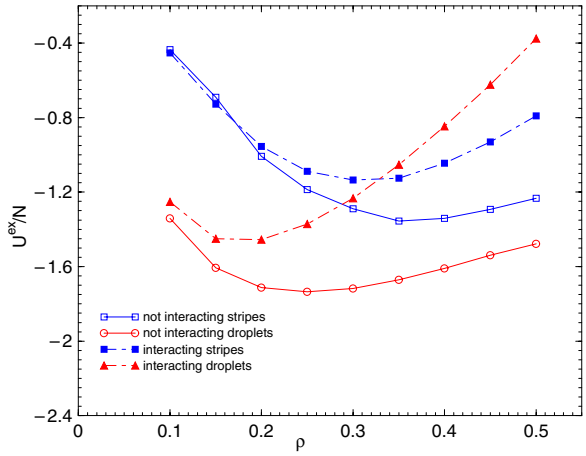

Figure 15. Model predictions concerning the droplets–stripes transition, with and without cluster–cluster repulsive interaction.

energy, which can be computed for a homogeneous fluid subject to a pairwise potential. To keep things very simple we neglect correlations, i.e. we put

$$\begin{aligned} &g(r) \sim 1, \\ &g_n^{(2)}(\mathbf{r}^1, \mathbf{r}^2) \sim 1. \end{aligned} \tag{15}$$

Remembering that $U^{\mathrm{ex}} = -\frac{\partial \ln Q}{\partial \beta}$ (Q: partition function) and that the free energy is $A = -\ln Q/\beta$, we can obtain an estimate of the free energy:

$$A = \frac{1}{\beta}\int_{\beta_0}^{\beta} U^{\mathrm{ex}}\,\mathrm{d}\beta = \frac{U^{\mathrm{ex}}(\beta - \beta_0)}{\beta}, \tag{16}$$

since the excess energy does not depend on the temperature in our approximation. β_0 is a reference state with respect to which we compute the change of free energy. Assuming that the reference state is the ideal one, such an approximation leads to $A^{\mathrm{ex}} = U^{\mathrm{ex}}$, so what we say for the excess internal energy can be immediately related to the free energy.

If in equation (12) we neglect the contribution u_{cc} due to interaction among clusters, we find that the circular domain should be preferred for all densities (see figure 15); in contrast, including u_{cc} we see that the results are totally different: there exist different density regions in which droplet patterns and striped patterns appear to be respectively preferred (figure 15), i.e. there exists a 'critical density ρ_0' such that for $\rho < \rho_0$ the system manages to minimize its excess internal energy (that, in our model, is equal to the free energy), setting particles into a droplet pattern, while for $\rho > \rho_0$ it achieves such energy minimization by setting particles into a striped pattern. Within this very simplified model, the passage between droplets and stripes happens at around $\rho_0 \sim 0.33$, consistent with our simulation evidence.

5. Microphases induced by external modulating potentials

If the intensity ϵ_{r} of the repulsive long-range potential in equation (2) is small, the system displays a standard liquid–vapour phase transition with a critical temperature which is a decreasing function of ϵ_{r}. The value of ϵ_{r} at which a fluid subject to competing interactions stops undergoing a standard liquid–vapour transition favouring a liquid-modulated phase is

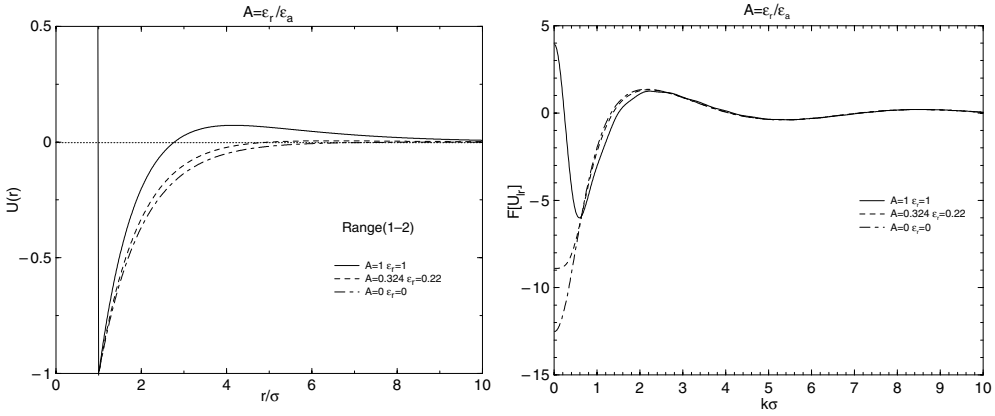

Figure 16. The interaction potential with different values of the parameters relating to the strength of the attractive and repulsive components (left) and its Fourier transform (right). The ranges of interactions are $R_a = 1\sigma$ and $R_r = 2\sigma$.

called the Lifshitz point (LP) [14]. In the RPA this point corresponds to a change of convexity of the Fourier transform of the interaction potential at zero wavevector. Theoretical studies of 3D systems [25] emphasize that, on approaching the LP (but without entering the microphase region yet), the inverse of the compressibility of the fluid has a very small value over an extended region in density and in temperature. That means that the system manages to achieve large density fluctuations without undergoing a phase transition. Such behaviour suggests that just in this region the presence of an external modulation should greatly affect the system. In this section we discuss such a situation for bidimensional systems. The interaction potential is the same as in equation (1): the ranges R_a and R_r have not been changed, while the intensities of the short-range and long-range interactions are $\epsilon_a = 0.679$ and $\epsilon_r = 0.22$. Such parameters correspond to the LP. In figure 16 we show the interaction potential and its Fourier transform for different values of $A = \epsilon_r/\epsilon_a$. We added, along the x direction, an external modulating potential of the form

$$U_m = -\epsilon_m \sum_i^N \cos^2\left(\frac{2\pi x_i}{\lambda}\right) \tag{17}$$

in which the strength ϵ_m is in units of the contact value U_c (defined in section 2), x_i refers to the i-particle abscissa; the period of the function is $P = \lambda/2$ which, in the present case, we have taken equal to half of the simulation box side. Simulations have been done adopting the MC_{cl} scheme (described in section 2) in a canonical ensemble and with $N = 400$ particles.

Adopting the random phase approximation described in section 4 we estimate the critical point position to be at $\rho_c \sim 0.28$ and $T_c \sim 0.95$. From simulation, we have verified that the fluid, without a modulating potential, undergoes a standard liquid–vapour transition below the critical point.

We studied a temperature range rather close to the estimated T_c along the critical isochore. Without external modulation and for $T \gtrsim T_c$ the fluid phase is characterized by a radial distribution function very slowly decaying to unity, as we can see from figure 17 where we plotted $g(r)$ for the thermodynamic state $\rho = 0.28$, $T = 1.1$ in comparison with a case relating to a bidimensional Lennard-Jones (LJ) system confirming the great influence of the density fluctuations in this particular region. On switching on the modulation, particles tend to organize in stripes located in correspondence with the minimum of the external potential

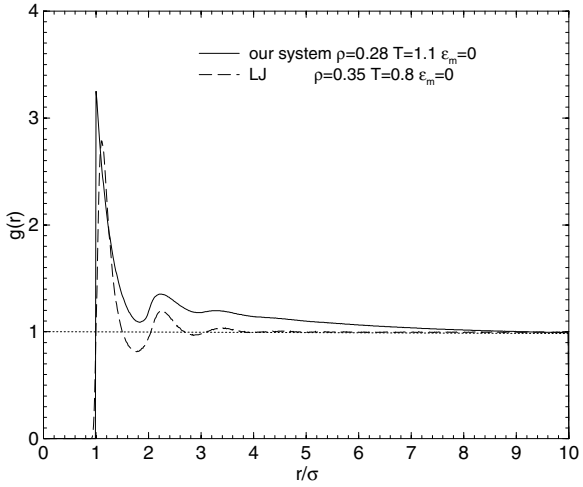

Figure 17. The radial distribution function for our system at the thermodynamic state $\rho = 0.28T = 1.1$ next to the LP compared with a typical behaviour of the same quantity for a classical LJ fluid (without external modulation).

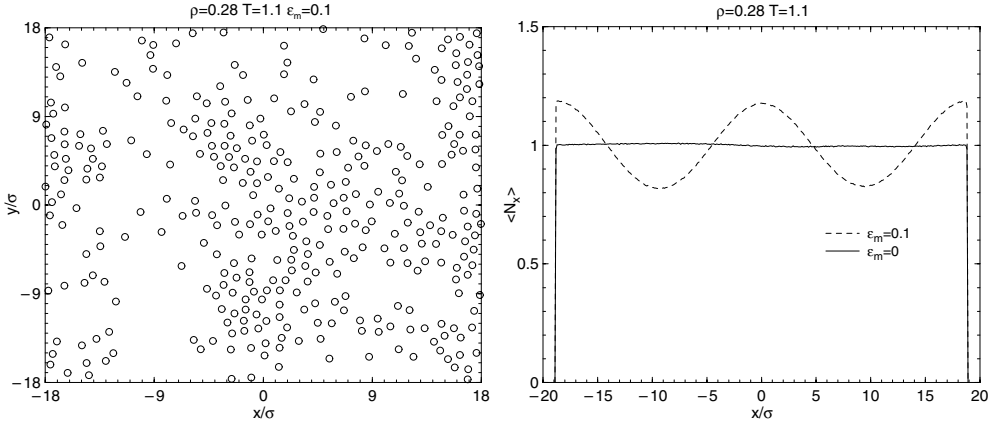

Figure 18. Left: a snapshot relating to our system for $\rho = 0.28T = 1.1$ and $\epsilon_{\rm m} = 0.1$. Right: number or particles versus position along the modulation axis normalized to the mean number of particles without an external potential.

(see figure 18 for a snapshot of the system and a typical density profile along the modulation direction). Obviously, a stripe pattern becomes better defined as $\epsilon_{\rm m}$ increases. In figure 19 an example of a structure factor is reported, with and without external modulation. For $\epsilon_{\rm m} = 0$, the x and y directions are equivalent since the fluid is homogeneous and isotropic; the large values of $S(k)$ at small k are due to the proximity of the critical point. For $\epsilon_{\rm m} = 0.1$ at $k\sigma \simeq 0.33$ (corresponding to the modulation wavevector of the external potential), $S(k)$ has increased particularly with respect to the counterpart computed along the y axis.

To test the effect of the density fluctuations close to the LP, we have compared our system with the bidimensional LJ one, studying the response to an external modulation at different temperatures and for various intensities of the external potential. To simplify the comparisons we have also expressed temperatures and modulation strengths in terms of the

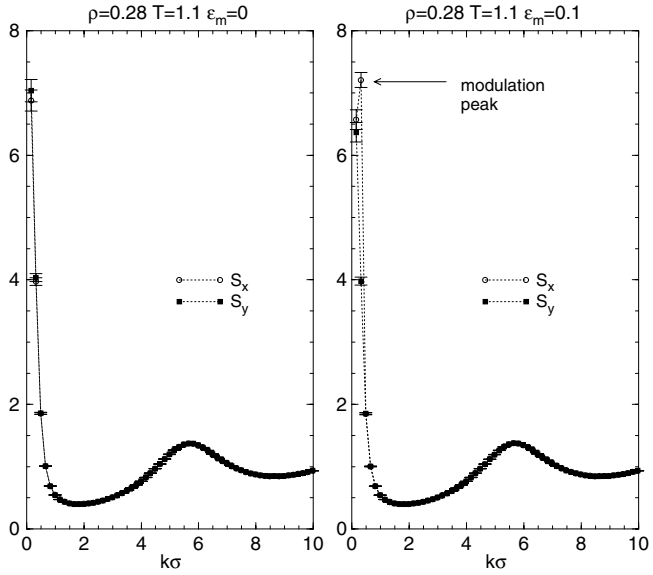

Figure 19. The static structure factor along the x and y directions without external modulation (left panel) and with external modulation (right panel); the position of the modulation peak is indicated. Dotted curves are only guides to the eyes.

Table 1. The temperature and external modulation strength, used in simulations for the LJ system, in units of the well depth and in units of the LJ critical temperature. See the text for explicit definitions.

T	t	$\epsilon_{\rm m}$	$\epsilon_{\rm m}^{\star}$
0.507	0.079	0.05	0.106
0.519	0.104	0.10	0.213
0.546	0.162	0.15	0.319
0.596	0.268		
0.800	0.702		

Table 2. The temperature and external modulation strength, used in simulations using our competing interaction potential, in units of both the contact value U_c and the critical temperature. See the text for explicit definitions.

T	t	$\epsilon_{\rm m}$	$\epsilon_{\rm m}^{\star}$
1.020	0.074	0.1	0.023
1.050	0.105	0.2	0.046
1.100	0.158	0.4	0.091
1.200	0.263		

critical temperature for each system. LJ data are collected in table 1, where $T \equiv k_{\rm B}T/w$ and $\epsilon_{\rm m} \equiv \epsilon_{\rm m}/w$ (w: depth of well), $t = (T - T_{\rm c}^{\rm LJ})/T_{\rm c}^{\rm LJ}$, $\epsilon_{\rm m}^{\star} = \epsilon_{\rm m} w/T_{\rm c}^{\rm LJ}$; estimations of the critical point for a LJ system in 2D can be found in the literature, according to which $\rho_{\rm c}^{\rm LJ} \sim 0.35$ and $T_{\rm c}^{\rm LJ} \sim 0.47$ [26]; for a critical review concerning the 2D LJ scenario, see also [27, 28]. Our system data are collected in table 2 where $t = (T - T_{\rm c})/T_{\rm c}$ and $\epsilon_{\rm m}^{\star} = \epsilon_{\rm m} U_{\rm c}/T_{\rm c}$.

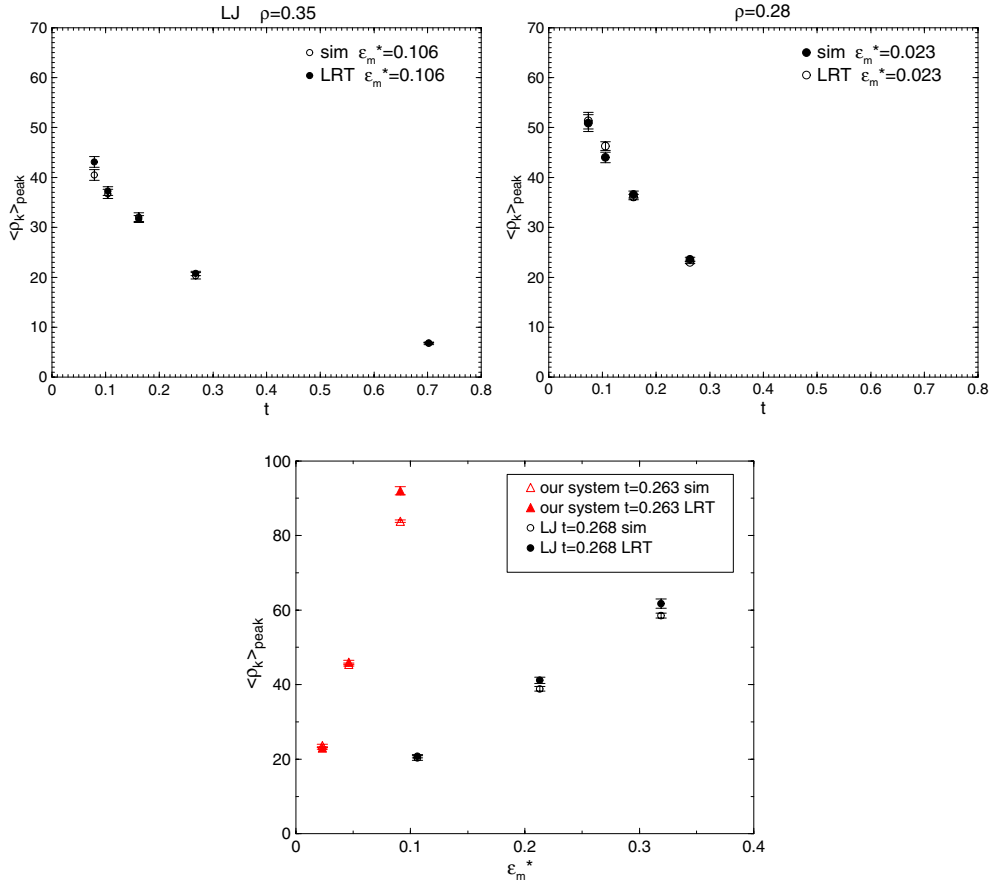

Figure 20. Upper panels: LRT predictions and simulation results concerning the Fourier transform of the density profile along the modulation axis; the correspondence at the modulation wavevector for a LJ fluid (left) and for our system (right), versus the reduced temperature $t = (T - T_c)/T_c$ at fixed $\epsilon_m^\star$. Bottom panel: LRT and simulation results versus $\epsilon_m^\star$ at fixed temperature. For each system, the temperatures and strengths of the modulating potential are expressed in units of the respective critical temperatures.

From simulations we computed the Fourier transform of the density profile along the modulation direction ($\langle\rho_k\rangle^{\rm sim}$). Then we applied the linear response theory (LRT) according to which

$$\langle\rho_k\rangle = \langle\rho_k\rangle_0 - \beta\rho S(k)_0 U_m(k), \tag{18}$$

where the subscript 0 denotes a canonical average over the unperturbed system and $U_m(k)$ is the Fourier component of the external potential at wavevector k; since the latter corresponds to a homogeneous fluid phase we can set $\langle\rho_k\rangle_0 = 0$. The static structure factor which appears in equation (18) has been estimated via simulation at $\epsilon_m = 0$ (after we had verified that $\langle\rho_k\rangle_0^{\rm sim} = 0$ within the errors). In the upper panels of figure 20 we plotted the results obtained for the LJ and for our system relating to the modulation wavevector as a function of temperature. In both cases we see that, for small modulation strength ϵ_m, LRT is a very good approximation even close to the critical point. In the bottom panel of figure 20 we plotted a comparison between LRT predictions and simulation data as a function of $\epsilon_m^\star$ for a given t: the response to

the external potential of the system with competing interaction is stronger than it is in the LJ system and the deviation from the linear theory starts at a smaller value of $\epsilon_{\mathrm{m}}^{\star}$. For example, in our case at $\epsilon_{\mathrm{m}}^{\star} = 0.091$, $\langle\rho_k\rangle_{\mathrm{peak}} \simeq 83$ and LRT is already not very accurate, while in the LJ system at $\epsilon_{\mathrm{m}}^{\star} = 0.106$, $\langle\rho_k\rangle_{\mathrm{peak}} \simeq 20$ and LRT still works very well. Obviously, if $\epsilon_{\mathrm{m}}^{\star}$ increases too much, LRT is no longer accurate for the LJ system either.

6. Conclusions

In this work we have presented detailed simulation data relating to the study of spontaneous pattern formation in bidimensional systems with competing short-range attractive and long-range repulsive interactions; we have shown that the PT technique is a promising approach, since this technique reaches equilibrium configurations faster than other algorithms and it improves the quality of the statistics. At the densities of our computations, we have observed the formation of droplet-like or stripe-like patterns. The location of the transition temperature from the modulated region to the homogeneous phase has been clearly identified via the position of the peak in the specific heat.

We have also analysed how the arising of patterns affects structural quantities such as $g(r)$ and $S(k)$. The radial distribution function exhibits a long-range modulation due to the underlying pattern, which is doomed to disappear as temperature increases. The main feature, in the static structure factor, is the appearance of peaks (modulation peaks) at small wavevector. In particular, for $\rho = 0.4$ at $T \leqslant T_{\mathrm{c}}$, $S(\mathbf{k})$, computed on the grid of small wavevectors, is anisotropic in $\mathbf{k}$ and has a twofold symmetry due to the breaking of symmetry that the system undergoes, while at $T > T_{\mathrm{c}}$, $S(\mathbf{k})$ is isotropic with a unique strong peak at small wavevector. This signals that strong density fluctuations are present at temperatures above T_{c} where no patterns are present. Besides this, in the striped case we observe in the $S(\mathbf{k})$ profile, at low temperatures, the presence of many peaks at wavevectors which are multiples of the modulation period. The origin of such harmonics can be traced back to the rather abrupt density variation between its maximum and minimum values. This effect could be checked through scattering experiments. Some harmonics peaks are also present at $\rho = 0.1$ in the droplet phase, but these peaks are weaker and wider.

In a small system, like ours, the direction of the striped pattern appears to be stabilized by the periodic boundary conditions; in contrast, in a very large system we expect the direction of the stripes to fluctuate over time. This should provide an important test determining the timescale of such fluctuations, since they might influence properties such as the birefringence that could be experimentally measured.

For the homogeneous state the random phase approximation works quite well in giving the position of the fluctuation peak and it is semiquantitative as regards its amplitude. While the RPA predicts only the existence of a region in which the fluid is unstable with respect to a density modulation, without giving any information on the pattern shape, it is interesting to note the presence of a critical point in the spinodal curve given by the RPA and that the critical density is in the region in which, via simulation, we observed the passage from droplets to stripes. Finally, a very simple model, for mimicking the droplet–stripe transition, has been described. The most relevant aspect is that the shape of the pattern can be used to optimize and reduce cluster reciprocal repulsion. The development of a microscopic theory able to describe the modulated phases is an important open issue.

Finally, we have studied the behaviour of the fluid when it is close to its Lifshitz point but still in a homogeneous phase in which it is strongly affected by density fluctuations. We have analysed the system response to the presence of an external agent, such as a modulating potential. Comparing the results with those derived for a standard LJ fluid, subject to the

same external modulation, we have seen that our system is much more strongly affected by the action of the field. In other words, near the Lifshitz point the fluid experiences large density fluctuations and so can be easily driven into a stable microphase by the presence of a very weak external potential.

Acknowledgments

We thank D Pini and D Galli for helpful discussions.

This work was supported by the INFM Parallel Computing Project and by the INFM Research Project PAIS2001-Sez.G.

References

[1] Seul M and Andelman D 1995 *Science* **267** 476
[2] Sear R P, Chung S W, Markovich G, Gelbart W M and Heath J R 1999 *Phys. Rev.* E **59** R6255
[3] Gelbart W M, Sear R P, Heath J R and Chaney S 1999 *Faraday Discuss.* **112** 299
[4] Brown J J, Porter J A, Daghlian C P and Gibson U J 2001 *Langmuir* **17** 7966
[5] Ghezzi F and Earnshaw J C 1997 *J. Phys.: Condens. Matter* **9** L517
[6] Piazza R, Pierno M, Vignati E, Venturoli G, Francia F, Mallardi A and Palazzo G 2003 *Phys. Rev. Lett.* **90** 208101
[7] Tanaka S and Ataka M 2002 *Phys. Rev.* E **65** 051804
[8] Götze I O, Brader J M, Schmidt M and Löwen H 2003 *Mol. Phys.* **101** 1651
[9] Wei Q H, Bechimger C, Rudhardt D and Leiderer P 1998 *Phys. Rev. Lett.* **81** 2606
[10] Weber J E, Goñi A R, Pusiol D J and Thomsen C 2002 *Phys. Rev.* E **66** 021407
[11] Andelman D, Brochard F, Knobler C and Rondelez F 1994 Structures and phase transitions in Langmuir monolayers *Micelles, Membranes, Microemulsions and Monolayers* ed W M Gelbart, A Ben Shaul and D Roux (New York: Springer) p 559
[12] De Bell K, MacIsaac A B and Whitehead J P 2000 *Rev. Mod. Phys.* **72** 225
[13] Muratov C B 2002 *Phys. Rev.* E **66** 066108
[14] Pini D, Jialin G, Parola A and Reatto L 2000 *Chem. Phys. Lett.* **327** 209
[15] Allen M P and Tildesley D J 1999 *Computer Simulation of Liquids* (Oxford: Clarendon)
[16] Tavares J M, Weis J J and Telo de Gama M M 2002 *Phys. Rev.* E **65** 061201
[17] Weis J J 2003 *J. Phys.: Condens. Matter* **15** s1471
[18] Frenkel D and Smit B 2001 *Understanding Molecular Simulation* (New York: Academic)
[19] Opps S B and Schofield J 2001 *Phys. Rev.* E **63** 056701
[20] Faller R, Yan Q and de Pablo J J 2002 *J. Chem. Phys.* **116** 5419
[21] Yamamoto R and Kob W 2000 *Phys. Rev.* E **61** 5473
[22] Truskett T M, Sastry S, Debenedetti P G and Stillinger F H 1998 *Phys. Rev.* E **58** 3083
[23] Baus M and Colot J L 1986 *J. Phys. C: Solid State Phys.* **19** L643
[24] Sear R P and Gelbart W M 1998 *J. Chem. Phys.* **110** 4582
[25] Selke W 1991 *Phase Transition and Critical Phenomena* vol 15, ed J L Lebowitz and C Domb (New York: Academic)
[26] Rovere M 1993 *J. Phys.: Condens. Matter* **5** B193
[27] Wilding N B and Bruce A D 1992 *J. Phys.: Condens. Matter* **4** 3087
[28] Wilding N B 1995 *Phys. Rev.* E **52** 602